

Asymmetric Ejecta Distribution of the Cygnus Loop revealed with Suzaku

Satoru KATSUDA¹, Hiroshi TSUNEMI¹, Emi MIYATA¹, Koji MORI², Masaaki NAMIKI¹,
Norbert NEMES¹
and

Eric D. MILLER³

¹*Department of Earth and Space Science, Graduate School of Science, Osaka University, 1-1
Machikaneyama, Toyonaka, Osaka 560-0043*

katsuda@ess.sci.osaka-u.ac.jp

²*Department of Applied Physics, Faculty of Engineering, University of Miyazaki, 889-2192*

³*Kavli Institute for Astrophysics and Space Research, Massachusetts Institute of Technology,
Cambridge, MA 02139, U.S.A.*

(Received 2007 May 31; accepted 2007 August 8)

Abstract

We observed a linearly sliced area of the Cygnus Loop from the north-east to the south-west with Suzaku in seven pointings. After dividing the entire fields of view (FOV) into 119 cells, we extracted spectra from all of the cells and performed spectral analysis for them. We then applied both one- and two-component non-equilibrium ionization (NEI) models for all of the spectra, finding that almost all were significantly better fitted by the two-component NEI model rather than the one-component NEI model. Judging from the abundances, the high- kT_e component must be the ejecta component, while the low- kT_e component comes from the swept-up matter. Therefore, the ejecta turn out to be distributed inside a large area (at least our FOV) of the Cygnus Loop. We divided the entire FOV into northern and southern parts, and found that the ejecta distributions were asymmetric to the geometric center: the ejecta of Si, S, and Fe seem to be distributed more in the south than in the north of the Cygnus Loop by a factor of ~ 2 . The degree of ejecta-asymmetry is consistent with that expected by recent supernova explosion models.

Key words: ISM: abundances – ISM: individual (Cygnus Loop) – ISM: supernova remnants – X-rays: ISM

1. Introduction

The asymmetry of a supernova (SN) explosion is considered to be a key point to understand the mechanism driving an SN explosion. The spectropolarimetry of young SNe revealed a non-spherical core of the SN explosion. The degree of departure from spherical symmetry is considered to be anti-correlated with the mass of the hydrogen envelope, i.e., the remaining hydrogen shell of the progenitor star (e.g., Leonard et al. 2006). In the extreme case of departure from spherical symmetry, for example Type-IIIn SN 1998S, the major-to-minor axis ratio of the explosion core is expected to be larger than 2.5, suggesting a highly asymmetric explosion mechanism, possibly mediated by jets (Wang et al. 2001). From theoretical aspects, recent SN explosion models generally show aspherical ejecta distributions may also be produced by convection (e.g., Herant et al. 1994; Burrows et al. 1995; Janka & Muller 1996) as well as hydrodynamical instabilities (e.g., Kifonidis et al. 2006; Burrows et al. 2007; Janka et al. 2007) during SN explosions.

After a SN explosion, the ejecta initially expand without deceleration (so-called “free expansion”) behind the forward shock wave, which sweeps up the interstellar medium (ISM). When the mass of the swept-up matter becomes comparable to that of the ejecta, the expansion is decelerated by the swept-up matter. The deceleration initiates a reverse shock propagating into the ejecta. Both the swept-up matter and the ejecta are hot enough to emit X-rays. The swept-up matter forms a shell structure, while the ejecta fill its interior. Therefore, we can attempt to address the ejecta distributions by observing the structure of supernova remnants (SNRs) in X-rays. In fact, ejecta-dominated X-ray emission are detected in many SNRs (e.g., Cas A: Hughes et al. 2000; Tycho: Decourchelle et al. 2001; Vela: Tsunemi et al. 1999; G292.0+1.8: Park et al. 2001). Recent deep Chandra X-ray observations of Cas A SNR have revealed a bipolar structure of Si-rich ejecta (Hwang et al. 2004; Laming et al. 2003), suggesting an asymmetric explosion with bipolar jets.

The Cygnus Loop is a nearby (540 pc: Blair et al. 2005) proto-typical middle-aged (~ 10000 yrs) SNR. A number of pieces of evidence that the SN explosion of the Cygnus Loop occurred in a preexisting cavity (e.g., McCray 1979; Levenson et al. 1999), suggesting that the Cygnus Loop was produced by a core-collapse SN. Since it is an evolved SNR, the ejecta-material is embedded in swept-up matter. Miyata et al. (1994) observed the northeast (NE) shell of the Loop with ASCA, and revealed the metal deficiency there. Recent Suzaku observations of this region confirm the metal deficiency there (Miyata et al. 2007). Although the reason for the metal deficiency is not yet understood, it can be safely stated that contamination of the ejecta-material is negligible in the rim regions. In contrast to the rim regions, ASCA detected evidence of Si-, S-, and Fe-rich plasma at the center portion of the Cygnus Loop (Miyata et al. 1998), which is thought to be ejecta. The relative abundances of the ejecta support that the idea that the Cygnus Loop was the result from a core-collapse SN, and that the progenitor

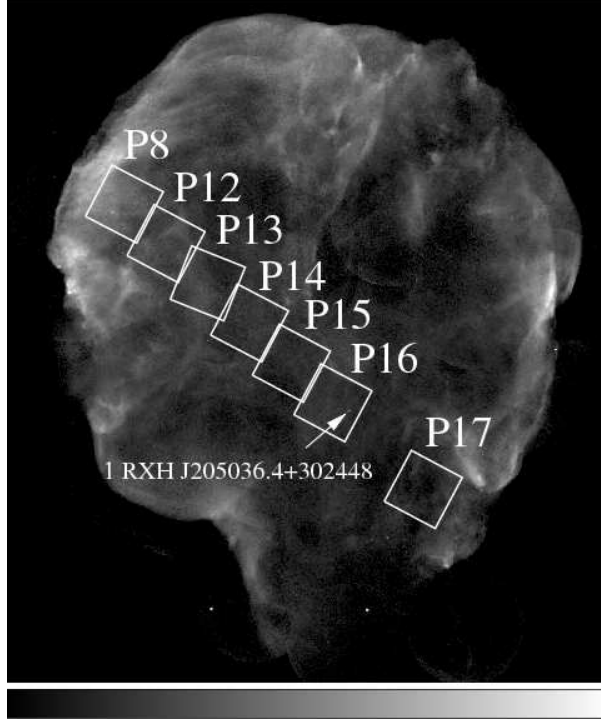


Fig. 1. ROSAT HRI image of the entire Cygnus Loop. The Suzaku FOV (P8, P12, P13, P14, P15, P16, and P17) are shown as white rectangles.

mass is estimated to be $25 M_{\odot}$ based on the central portion of the Cygnus Loop (Miyata et al. 1998). Recent XMM-Newton observations across the Cygnus Loop from the NE rim to the SW rim revealed ejecta distributed inside of $\sim 0.85 R_s$ of the Cygnus Loop, where R_s is the shock radius (Tsunemi et al. 2007). The relative abundances inferred for the total ejecta are almost consistent with those expected for the core-collapse SN, whose progenitor mass is $13 M_{\odot}$ (Katsuda & Tsunemi 2008), which can be considered to be more reliable than that estimated from the ASCA observation, since the coverage of the total FOV of the XMM-Newton observations is about an order of magnitude larger than that of the ASCA observation, giving a more representative sample of the ejecta abundances to compare with theoretical models.

Since the Cygnus Loop is very large in apparent size ($2^{\circ}5 \times 3^{\circ}5$: Levenson et al. 1997; Aschenbach & Leahy 1999), it is an ideal target to study the spatial distribution of the ejecta material. In order to reveal ejecta structures in this SNR, we observed the Cygnus Loop from the NE rim to the SW rim with Suzaku (Mitsuda et al. 2007). We selected our fields of view (FOV) so as to cover just southern regions of the XMM-Newton observation path since the distribution of Si-, S-, and Fe-rich ejecta is suggested to be elongated toward the south of the Loop (Tsunemi et al. 2007).

Table 1. Information of observations of the Cygnus Loop and Lockman Hole.

Obs. ID	Coordinate (RA, DEC)	Roll	Obs. Date	Effective Exposure
Cygnus Loop				
501028010 (P8)	314.005, 31.464	58.5	2006.05.13	4.7 ks
501029010 (P12)	313.751, 31.263	58.7	2006.5.09	13.2 ks
501030010 (P13)	313.498, 31.061	58.9	2006.05.10	13.9 ks
501031010 (P14)	313.245, 30.859	59.1	2006.5.12	18.2 ks
501032010 (P15)	312.993, 30.653	59.3	2006.05.25	17.4 ks
501033010 (P16)	312.745, 30.450	59.5	2006.05.22	20.0 ks
501034010 (P17)	312.207, 30.005	60.0	2006.05.22	13.9 ks
Lockman Hole				
101002010	162.938, 57.267	32.7	2006.05.17	69.0 ks

2. Observations and Data Screening

The observations comprised seven pointings: P8, P12, P13, P14, P15, P16, and P17. The FOV of our Suzaku observations are shown in figure 1. We employed revision 1.2 of the cleaned event data. We excluded data taken in the low cut-off rigidity < 6 GV. As a background, we used a spectrum obtained from the Lockman Hole because its observation date, 2006 May 17 was close to those of the Cygnus Loop. Obs. IDs, the nominal point, roll angle, observation date, and the effective exposure times after the screening are summarized in table 1. Figure 2 shows a merged XIS1 (back-illuminated CCD; BI CCD) three-color image. Red, green, and blue colors correspond to narrow energy bands of 0.54–0.59 keV (O VII $K\alpha$), 0.88–0.94 keV (Ne IX $K\alpha$), and 0.69–0.85 keV (Fe L), respectively. We can see strong blue color around the center portion (i.e., P15 and P16), whereas red and green colors are enhanced in the NE regions (i.e., P8 and P12). For spectrum fitting, we used photons in the energy ranges of 0.2–3.0 keV and 0.4–3.0 keV for XIS1 and XIS0, 2, 3 (front-illuminated CCD; FI CCD), respectively.

3. Spatially Resolved Spectral Analysis

We divided the entire FOV into 119 rectangular small cells, indicated in figure 2, such that each cell contained 2500–5000 photons for XIS0 to equalize the statistics. The sizes of small cells ranged from 1/32 FOV to 1/8 FOV. We then extracted spectra from them. Generally, count rates above 2 keV were so low that the statistics were too poor in each cell. It is quite difficult to constrain the abundance of S. Therefore, by dividing each FOV into the NE part and the SW part, we accumulated photons in the energy range above 2 keV from the NE or SW half, where each small cell was included, whereas we extracted spectra below 2 keV from each small cell. Example regions in each FOV, a black cell for < 2 keV and a green cell for > 2 keV,

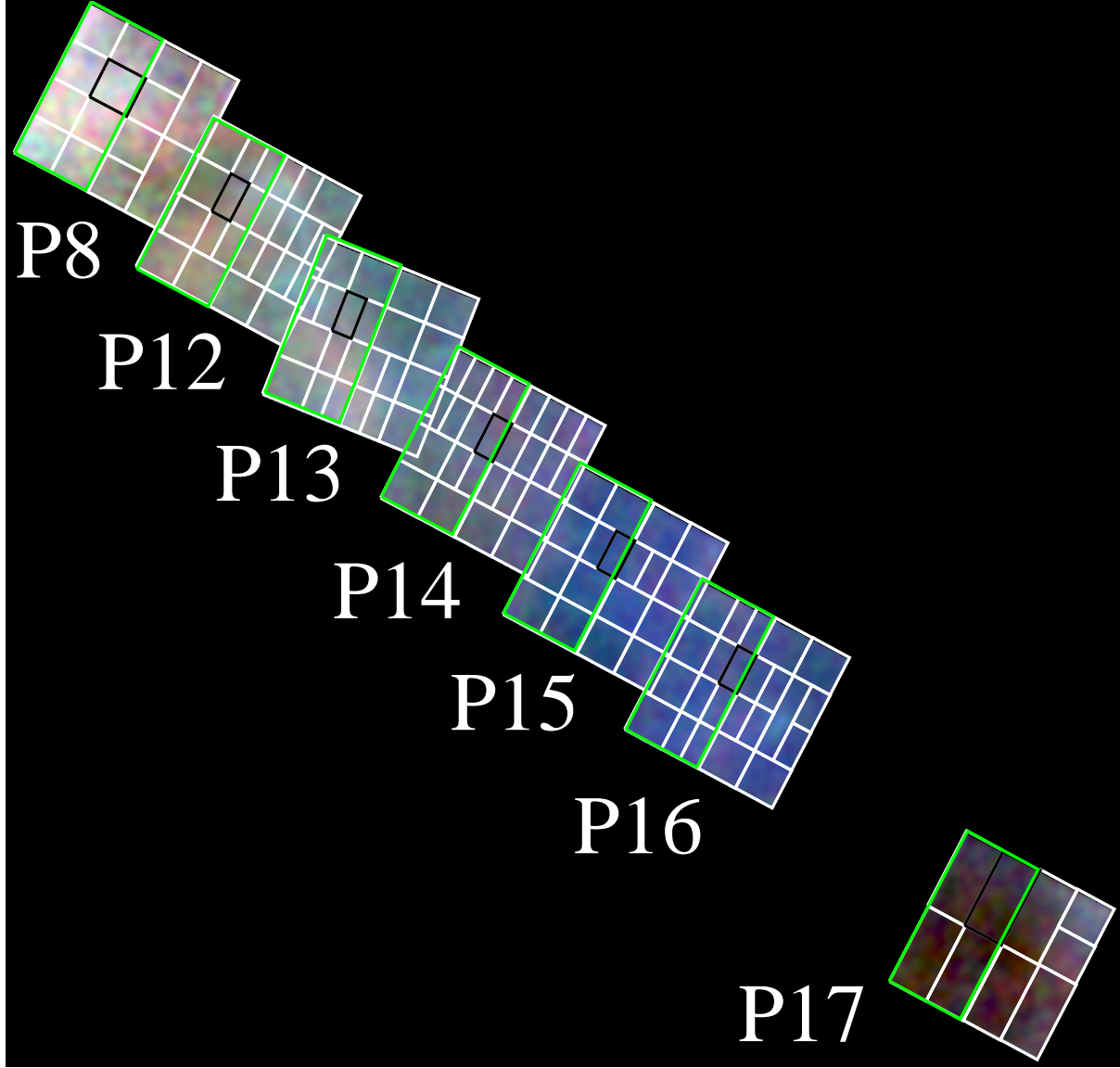


Fig. 2. Three-color image merged by seven XIS FOV (Red: O VII $K\alpha$, Green: Ne IX $K\alpha$, Blue: Fe L). The data were binned by 8 pixels and smoothed by a Gaussian kernel of $\sigma = 25''$. The effects of exposure, vignetting, and contamination are corrected. Small rectangles were the cells where we extracted spectra. We show example spectra from black cells for <2 keV and green cells for >2 keV in figure 3.

are shown in figure 2. In this way, we obtained much better constraints on the S abundance for each cell than those determined by fitting entire-energy-band spectra extracted from each small cell. The S abundances were different for each small cell due to the spectral differences below 2 keV. To generate the response matrix file (RMF) and the ancillary response file (ARF), we employed `xisrmfgen` and `xissimarfgen` (Ishisaki et al. 2007) (version 2006-10-26), respectively. The low-energy efficiency of the XIS shows degradation caused by contaminants accumulated on the optical blocking filter (Koyama et al. 2007), which was taken into account generating of the ARF file.

Firstly, all spectra were fitted by an absorbed non-equilibrium ionization (NEI) model with a single component [the wabs; Morrison & McCammon 1983 and the VNEI model (NEI version 2.0); e.g., Borkowski et al. 2001 in XSPEC v 11.3.1]. Free parameters are the hydrogen column density in cm^{-2} , N_{H} ; electron temperature in keV, kT_{e} ; the ionization time, τ , where τ is the electron density in cm^{-3} times the elapsed time in sec after the shock heating; the emission measure, EM ($\text{EM} = \int n_{\text{e}} n_{\text{H}} dl$, where n_{e} and n_{H} are the number densities of electrons and hydrogens in cm^{-3} , respectively and dl is the plasma depth in cm); the abundances of C, N, O, Ne, Mg, Si, S, Fe, and Ni. We set abundance of Ni to be equal to that of Fe. The abundances of other elements included in the VNEI model (i.e., Ar and Ca) were fixed to the solar values (Anders & Grevesse 1989). An example spectrum from the black cell in P16, shown in Figure 2, is presented in figure 3, indicated as P16 (left) together with the best-fit model. This model gave us quite good fits, except for the energy bands around Si- and S-K lines where we can see a large discrepancy between our data and the model. Since the emission from both the ejecta and the swept-up matter were detected as a projection effect around the center portion of the Cygnus Loop (Miyata et al. 1998; Tsunemi et al. 2007; Katsuda & Tsunemi 2008), it is natural to consider that we need at least two (i.e., the swept-up matter and the ejecta) components to reproduce our data.

We then applied a two-component NEI model for all spectra. In this model, kT_{e} , τ , and EM are free parameters for both components. N_{H} is also left as a free parameter, but tied in the two components. Assuming that the swept-up matter surrounds the ejecta, we fixed the metal abundances for the swept-up matter component to those of the NE rim regions of the Cygnus Loop, where we expect no ejecta component (Uchida et al. 2006). The metal abundances are described in the footnote of table 2. Then, we left the metal abundances of O(=C=N), Ne, Mg, Si, S, and Fe(=Ni) for the ejecta component as free parameters. We confined the values of N_{H} in the range from 0.01 to $0.06 \times 10^{22} \text{ cm}^{-2}$ (Inoue et al. 1980; Miyata et al. 2007). Figure 3 shows example spectra from seven black cells shown in figure 2. We summarize the best-fit parameters for the example spectra in table 2. Based on table 2, we found that the two components clearly showed different temperature with each other. The low- kT_{e} component was responsible for the swept-up matter while the high- kT_{e} component was responsible for another component. We found that the metal abundances for at least one element of the high- kT_{e} component were about

an order-of-magnitude higher than those for the low- kT_e component, which clearly showed that the high- kT_e component represented the ejecta component. In this way, we performed spectral fittings for all spectra from 119 small cells. Applying the F -test with a significance level of 99%, we found that this model gave us better fits than those for one-component NEI models for almost all of the spectra [e.g., from figure 3 P16 (left) to P16 (right)]. We obtained fairly good fits for all spectra by the two-component NEI model (reduced $\chi^2 < 1.7$). If we consider the calibration uncertainty of the energy scale (± 5 eV; Koyama et al. 2007), the values of reduced χ^2 become lower than 1.4. Nonetheless, the fits are not acceptable for many spectra from a statistical point of view, which suggests that our model is too simple. However, we believe that the two-component model is a good approximation to represent our data. Taking into consideration that the spectra from almost all cells require the two-component model, the ejecta turned out to be distributed inside a large fraction (at least our FOV) of the Cygnus Loop. Since the outer edge of our FOV is located around $0.85 R_s$, our result matches the view from XMM-Newton observations that the ejecta are distributed inside $\sim 0.85 R_s$ of the Cygnus Loop.

Figure 4 shows maps of the best-fit parameters obtained from the two-component NEI model. The subscript, H, denotes the high- kT_e , i.e., the ejecta component while L denotes the low- kT_e , i.e., the swept-up matter component. We showed EMs of O, Ne, Mg, Si, S, and Fe for the ejecta component. We marked the geometric center of the Cygnus Loop (RA=20^h51^m19^s, DEC=31°02'48" [J2000]: Ku et al. 1984) as a white dot in each figure. There is a point source, 1RXH J205036.4 + 302448, within P16 (see, figure 1). We excluded the responsible cell from our analysis, which can be seen as a black box in the map of $\log(\tau_H)$ shown in figure 4. N_H s tend to show relatively large values around the center in each FOV to those in the edge regions. Since such N_H variations must be due to the contamination problem of the XIS (Koyama et al. 2007), the current model of a spatial variation of the contaminants accumulated on the optical blocking filter should be modified properly. We found that the value of kT_e for the swept-up matter component is ~ 0.2 keV in our entire FOV other than P15 and P16, where we can see slightly higher values (~ 0.3 keV). The values of kT_e for the ejecta component show a significant variation from the SW (~ 0.35 keV) to the NE (~ 0.7 keV) portion in our FOV as Miyata et al. (2000) already noted the hard X-ray-emitting region in the NE portion by ASCA GIS observations and suggested that the hard X-ray might come from the ejecta. The collisional ionization equilibrium (CIE) has already been established for both components in most cells in P17, which seems consistent with the results from Chandra observations of the SW rim of the Cygnus Loop (Leahy 2004).

We noticed a clear anti-correlation between kT_{eH} and τ_H , and a correlation between τ_H and EMs of Si, S, and Fe in the ejecta component. We examined the systematic effect between the ionization age (and/or temperature) and the distributions of the Si-, S-, and Fe-ejecta. We re-fitted the example spectrum in P15, employing the same two-component model used in this

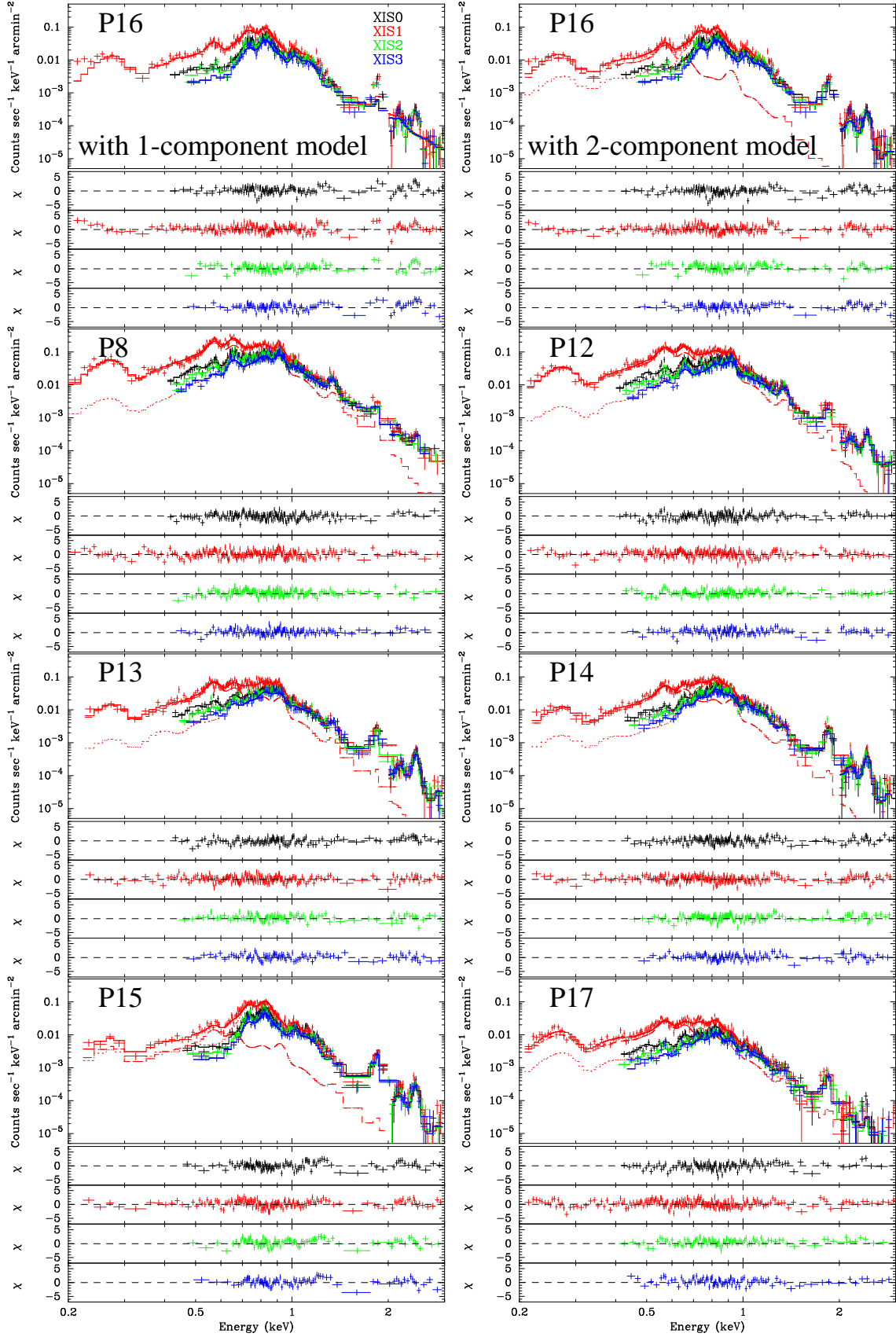


Fig. 3. Top-left panel: X-ray spectra extracted from the black cell in P16 indicated in figure 2. The best-fit curves for one-component NEI model are shown with solid lines and the lower panels show the residuals. The small gap around 2 keV is due to the fact that we extracted spectra below 2 keV from each small cell, while above 2 keV from half of each FOV. Top-right panel: Same as top left but with two-component NEI best-fit models. The contribution of each component is shown by the dotted lines

Table 2. Spectral-fit parameters for the example spectra.

Parameter	P8	P12	P13	P14	P15	P16	P17
$N_{\text{H}}[\times 10^{22} \text{cm}^{-2}]$	$0.044^{+0.005}_{-0.003}$	$0.049^{+0.005}_{-0.003}$	0.060 ± 0.004	0.060 ± 0.004	$0.049^{+0.006}_{-0.003}$	0.060 ± 0.003	0.031 ± 0.002
High temperature component							
$kT_{\text{e1}}[\text{keV}]$	0.55 ± 0.01	$0.73^{+0.03}_{-0.01}$	0.60 ± 0.04	0.60 ± 0.04	0.38 ± 0.01	0.39 ± 0.01	0.35 ± 0.01
O(=C=N)	0.9 ± 0.1	0.6 ± 0.1	$0.47^{+0.09}_{-0.08}$	1.2 ± 0.4	0.30 ± 0.05	0.5 ± 0.1	0.20 ± 0.05
Ne	0.8 ± 0.1	0.7 ± 0.1	0.8 ± 0.2	0.7 ± 0.2	0.29 ± 0.06	$0.46^{+0.07}_{-0.08}$	0.15 ± 0.05
Mg	0.5 ± 0.1	0.5 ± 0.1	0.8 ± 0.2	0.6 ± 0.2	0.16 ± 0.09	0.14 ± 0.09	0.14 ± 0.09
Si	0.6 ± 0.2	1.0 ± 0.2	5.1 ± 0.6	6.1 ± 0.7	3.6 ± 0.4	4.1 ± 0.4	$2.7^{+0.5}_{-0.6}$
S	1.2 ± 0.4	2.8 ± 0.5	10 ± 1	11 ± 1	7.1 ± 0.9	7.5 ± 0.8	4 ± 3
Fe(=Ni)	$0.62^{+0.06}_{-0.08}$	1.1 ± 0.1	3.3 ± 0.1	3.9 ± 0.2	2.04 ± 0.04	2.30 ± 0.05	0.75 ± 0.03
$\log(\tau_1/\text{cm}^{-3} \text{s})$	$11.2^{+0.04}_{-0.09}$	$10.73^{+0.06}_{-0.04}$	$11.11^{+0.07}_{-0.11}$	11.5 ± 0.1	$11.76^{+0.10}_{-0.07}$	$11.76^{+0.08}_{-0.09}$	$12.0^{+1.7}_{-0.2}$
$\text{EM}_1^{\dagger}[\times 10^{19} \text{cm}^{-5}]$	0.22 ± 0.01	$0.072^{+0.006}_{-0.005}$	0.043 ± 0.001	0.061 ± 0.002	0.166 ± 0.003	0.131 ± 0.002	0.102 ± 0.003
Low temperature component							
$kT_{\text{e2}}[\text{keV}]$	0.24 ± 0.01	0.23 ± 0.01	0.23 ± 0.01	0.21 ± 0.01	0.18 ± 0.01	0.15 ± 0.01	0.22 ± 0.01
Abundances	(fixed to those determined for the NE rim of the Cygnus Loop) [‡]						
$\log(\tau_2/\text{cm}^{-3} \text{s})$	11.33 ± 0.04	11.3 ± 0.1	11.21 ± 0.05	$11.67^{+0.09}_{-0.08}$	$13.1^{+0.6}_{-1.1}$	$12.0^{+1.7}_{-0.2}$	11.58 ± 0.04
$\text{EM}_2^{\dagger}[\times 10^{19} \text{cm}^{-5}]$	$4.4^{+0.2}_{-0.1}$	$2.8^{+0.1}_{-0.2}$	1.91 ± 0.06	$2.16^{+0.10}_{-0.09}$	0.67 ± 0.05	$1.5^{+0.2}_{-0.1}$	0.63 ± 0.01
$\chi^2/\text{d.o.f.}$	772/643	749/617	524/492	653/576	654/459	751/525	769/523

*Other elements are fixed to those of solar values.

The values of abundances are multiples of solar value.

The errors are in the range $\Delta\chi^2 < 2.7$ on one parameter.

[†] EM denotes the emission measure, $\int n_e n_{\text{H}} dl$.

[‡] C=0.27, N=0.10, O=0.11, Ne=0.21, Mg=0.17, Si=0.34, S=0.17, and Fe(=Ni)=0.20 (Uchida et al. 2006).

paper, but with a fixed ionization age of $1 \times 10^{11} \text{cm}^{-3} \text{s}$ for the ejecta component (which is the typical value in P8, 12, 13). We noticed a slight increase of kT_{eH} that is still significantly lower than that in the northern part of our FOV. We found that the emission measures of Si, S, and Fe were, respectively, reduced by 30%, 30%, and 15% from those obtained in the case that we left the ionization age as a free parameter. These values are still higher than those obtained in P8, 12, and 13 by $\sim 50\%$. Therefore, we can safely conclude that the EMs of Si-, S-, and Fe-ejecta in the southern part of our FOV are higher than those in the northern part of our FOV.

The ionization states for the ejecta component in P15 and P16 also reached the CIE condition. Apart from P15, P16, and P17, the ionization states for both components are in NEI condition in almost all of the cells. We found that all of the elements were distributed asymmetric to the geometric center. The EMs for O, Ne, and Mg are enhanced in P8 while no

Table 3. Summary of EI ($= \int n_e n_i dV$ for the ejecta component in units of 10^{52} cm^{-3}) in each FOV.*

Elements	P8	P12	P13	P14	P15	P16	P17
O	$5.3^{+0.8}_{-0.7}$	2.4 ± 0.4	2.6 ± 0.4	$2.0^{+2.3}_{-1.0}$	2.9 ± 0.6	3.0 ± 0.5	1.8 ± 0.2
Ne	1.2 ± 0.1	$0.50^{+0.09}_{-0.08}$	0.26 ± 0.08	0.26 ± 0.12	0.44 ± 0.09	0.51 ± 0.08	0.30 ± 0.05
Mg	0.26 ± 0.05	0.12 ± 0.02	0.10 ± 0.03	$0.06^{+0.05}_{-0.03}$	$0.036^{+0.038}_{-0.025}$	0.03 ± 0.02	0.06 ± 0.03
Si	0.25 ± 0.10	0.24 ± 0.03	0.49 ± 0.06	0.7 ± 0.1	1.3 ± 0.2	1.2 ± 0.1	0.5 ± 0.2
S	0.18 ± 0.07	0.23 ± 0.03	0.40 ± 0.04	0.63 ± 0.06	0.9 ± 0.1	0.9 ± 0.1	$0.18^{+0.10}_{-0.09}$
Fe	0.24 ± 0.04	0.29 ± 0.02	0.44 ± 0.01	0.57 ± 0.02	0.89 ± 0.02	0.82 ± 0.02	0.30 ± 0.01

*Errors quoted are the mean 90% confidence level for each cell.

enhancements are seen for the other elements there. Also, the EMs for all the elements other than Mg show enhancements in P15 and P16.

We obtained EMs of O, Ne, Mg, Si, S, and Fe for the ejecta component in 119 cells. Multiplying the EM by the area of each cell, we obtained the emission integral (hereafter EI, $\text{EI} = \int n_e n_H dV$, dV is the X-ray-emitting volume) of all elements for each cell, and summed up the EIs for all cells within each FOV. The summed-up EIs are summarized in table 3.

4. Discussion and Conclusions

We observed the Cygnus Loop from NE to SW with Suzaku in seven pointings. Dividing the entire FOV into 119 cells, we extracted spectra from all of the cells, and performed spectral analyses for them. Almost all of the spectra were significantly better fitted by a two-component NEI model, rather than a one-component NEI model. Judging from the abundances, the high- kT_e component must be ejecta, while the low- kT_e component comes from the swept-up matter.

4.1. Swept-up-Matter Distribution

The temperature for the swept-up matter component is significantly lower than that for the ejecta component. On the other hand, it is similar to that obtained for the rim of the Loop, where we expect no contamination of the ejecta (e.g., Miyata et al. 2007). Therefore, we believe that we surely separated the X-ray emission of the ejecta inside the Loop from that of the surrounding matter. The EM distribution of the swept-up matter (EM_L) is inhomogeneous in our FOV, as shown in figure 4. The shell of the swept-up matter seems to be thin in the SW part (i.e., P15 and P16) of the Loop relative to that in the NE part. Such a trend is also reported by XMM-Newton observations covering just north of our Suzaku path (Tsunemi et al. 2007). As Tsunemi et al. (2007) mentioned, there might be a blowout in the direction of our line of sight around P15 and P16, such as a south blowout of the Loop (see, figure 1). The relatively high temperature in P15 and P16 suggests that the velocity of the blast wave is higher than that in the other regions. This fact indicates that the density of ambient matter

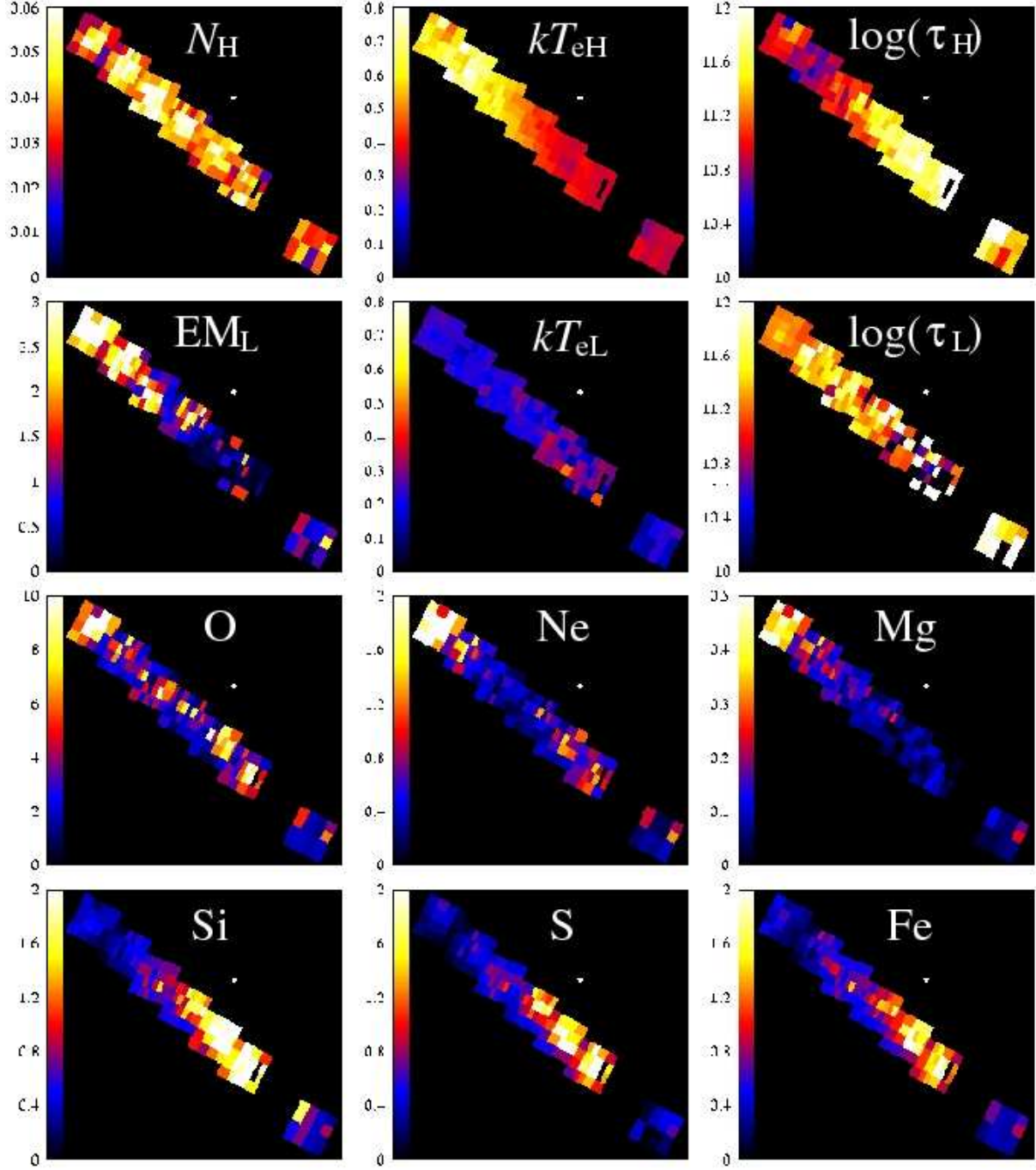


Fig. 4. Maps of the best-fit parameters. The values of N_H , kT_e , EM_L are in units of 10^{22}cm^{-2} , keV, and 10^{19}cm^{-5} , respectively. Lower six maps show EMs of O, Ne, Mg, Si, S, and Fe for the high- kT_e component in units of 10^{14}cm^{-5} . We adjusted the color code, such that we can see the differences in each figure.

in P15 and P16 is lower than that in the other regions, supporting the thin swept-up-matter shell.

4.2. *Metal Distribution in Ejecta Component*

We divided our FOV into two parts: the NE part (P8, P12, P13, and P14) and the SW part (P15, P16, and P17). There is a gap between P16 and P17, which we did not observe. Assuming EIs of the ejecta in the gap to be averages of those in P16 and P17, we calculated the ratios between EIs in the NE part and those in the SW part. They are $O \sim 1.2$, $Ne \sim 1.3$, $Mg \sim 3.2$, $Si \sim 0.44$, $S \sim 0.57$, and $Fe \sim 0.60$. For simplicity, we assumed that the mass ratios of those elements are equal to the EI ratios. Regarding the O-Ne group, similar amounts of those elements exist in the NE and SW parts. In contrast to the O-Ne group, the other elements show non-uniform distributions: Mg is distributed more in the NE part by a factor of ~ 3 , while Si, S, and Fe are distributed more in the SW part by a factor of ~ 2 . (Note that the mass ratio being proportional to a product of the density times the emitting volume will be lower than that of the EI ratio.)

A natural explanation for the asymmetries is an asymmetry at the time of the SN explosion of the Cygnus Loop. The degree of north-south (1:2) asymmetry of the innermost ejecta, such as Si-, S-, and Fe-ejecta, is consistent with that expected from asymmetric explosions resulting from hydrodynamic instabilities, which are described in recent theoretical models of SN explosions (e.g., Burrows et al. 2007). However, we should keep in mind that there are some other possibilities that can produce the asymmetries of the ejecta. The X-ray emission is sensitive to both temperature and density, i.e., dense ejecta emit more strongly than do thin ejecta and cooled ejecta will not continue to emit X-rays. Furthermore, an asymmetric environment that might be created by stellar winds (e.g., Blondin et al. 1996; Dwarkadas 2007) as well as hydrodynamic instabilities during the remnant evolution (Jun & Norman 1995) can make the ejecta distribution distorted.

If the mass ejection were to be anisotropic, it would lead a recoil of a stellar remnant due to momentum conservation. Therefore, we expect to see the velocity of the stellar remnant directed opposite to the momentum of the gaseous SN ejecta (e.g., Scheck et al. 2006). In fact, recent observations of a stellar remnant in Puppis A SNR revealed that its velocity was very high ($>1000 \text{ km sec}^{-1}$) and directed opposite to the momentum of fast-moving O-rich ejecta (Winkler & Petre 2006; Hui & Becker 2006). Since the Cygnus Loop is believed to be a remnant of a core-collapse SN explosion, the presence of a stellar remnant is strongly expected. So far, we have not found any stellar remnant associated with the SN explosion of the Cygnus Loop (e.g., Miyata et al. 2001). Taking into consideration that the momentum of innermost ejecta (which is considered to be strongly related to the stellar remnant) seems to be directed toward south of the Loop, we might find the stellar remnant associated with the Cygnus Loop in the north of the Loop. We observed the Cygnus Loop from the NE rim to the SW rim

with Suzaku as well as XMM-Newton. The observation paths covered about one seventh of the entire Loop. Further, Suzaku and/or XMM-Newton observations of the rest of the area are required to obtain the relative abundances for the total ejecta as well as to reveal the ejecta structure in the entire Loop.

This work is partly supported by a Grant-in-Aid for Scientific Research by the Ministry of Education, Culture, Sports, Science and Technology (16002004). This study is also carried out as part of the 21st Century COE Program, 'Towards a new basic science: depth and synthesis'. S. K. is supported by a JSPS Research Fellowship for Young Scientists.

References

- Anders, E., & Grevesse, N. 1989, *Geochim. Cosmochim. Acta*, 53, 197
- Aschenbach, B. & Leahy 1999, *A&A*, 341, 602
- Blair, W. P., Sankrit, R., & Raymond, J. C. 2005, *AJ*, 129, 2268
- Blondin, J. M., Lundqvist, P., & Chevalier, R. A. 1996, *ApJ*, 472, 257
- Borkowski, K. J., Lierly, W. J., & Reynolds, S. P. 2001, *ApJ*, 548, 820
- Burrows, A., Hayes, J., & Fryxell, B. A. 1995, *ApJ*, 450, 830
- Burrows, A., Livne, E., Dessart, L., Ott, C. D., Murphy, J. 2007, *ApJ*, 655, 416
- Decourchelle, A., et al. 2001, *A&A*, 365, L218
- Dwarkadas V. V. 2007, *Ap&SS*, 307, 153
- Herant, M., Benz, W., Hix, W. R., Fryer, C. L., & Colgate, S. A. 1994, *ApJ*, 435, 339
- Hughes, J. P., Rakowski, C. E., Burrows, D. N., Slane, P. O. 2000, *ApJ*, 528, L109
- Hui, C. Y., & Becker, W. 2006, *A&A*, 454, 543
- Hwang, U. et al. 2004, *ApJ*, 615, L117
- Inoue, H., Koyama, K., Matsuoka, M., Ohashi, T., Tanaka, Y., & Tsunemi, H. 1980 *ApJ*, 238, 886
- Ishisaki, Y., et al. 2007, *PASJ*, 59, S113
- Janka, H. T & Müller, E. 1996, *A&A*, 306, 167
- Janka, H. -Th., Marek, A., Kitaura, F.-S. 2007, *astro-ph/0706.3056*
- Jun, B. -I., & Norman, M. L. 1995, *Ap&SS*, 233, 267
- Katsuda, S. & Tsunemi, H. 2008, *Adv. Space Res.* in press
- Kifonidis, K., Plewa, T., Scheck, L., Janka, H.-T., & Müller, E. 2006, *A&A*, 453, 661
- Koyama, K. et al. 2007, *PASJ*, 59, S221
- Ku, W. H. -M., Kahn, S. M., Pisarski, R., & Long, K. S. 1984, *ApJ*, 278, 615
- Laming, J. M., & Hwang, U., 2003, *ApJ*, 597, L347
- Leonard D. C. et al. 2006, *Nature*, 440, 505
- Levenson, N. A., et al. 1997, *ApJ*, 484, 304
- Levenson, N. A., Graham, J. R., & Snowden, S. L. 1999, *ApJ*, 526, 874
- Leahy, D. A. 2004, *MNRAS*, 351, 385
- McCray, R., & Snow, T. P., Jr. 1979, *ARA&A*, 17, 213
- Miyata, E., Tsunemi, H., Pisarski, R., & Kissel, S. E. 1994, *PASJ*, 46, L101

- Miyata, E., Tsunemi, H., Kohmura, T., Suzuki, S., & Kumagai, S. 1998, PASJ, 50, 257
- Miyata, E., Tsunemi, H., Koyama, K., & Ishisaki, Y. 2000, Adv. Space Res., 25, 555
- Miyata, E., Ohta, K., Torii, K., Takeshima, T., Tsunemi, H., Hasegawa, T., & Hashimoto, Y. 2001, ApJ, 550, 1023
- Miyata, E., Katsuda, S., Tsunemi, H., Hughes, J. P., Kokubun, M., & Porter, F. S. 2007, PASJ, 59, S163
- Mitsuda, K., et al. 2007, PASJ, 59, S1
- Morrison, R., & McCammon, D. 1983, ApJ, 270, 119
- Park, S., Roming, P. W. A., Hughes, J. P., Slane, P. O., Burrows, D. N., Garmire, G.P. & Nousek, J. A. 2002, ApJ, 564, L39
- Scheck, L., Kifonidis, K., Janka, H.-T., Müller, E. 2006, A&A, 457, 963
- Tsunemi, H., Miyata, E., & Aschenbach, B. 1999, PASJ, 51, 711
- Tsunemi, H., Katsuda, S., & Nemes, N., & Miller, E. D. 2007 ApJ in press submitted to ApJ
- Uchida, H. Katsuda, S., Miyata, E., Tsunemi, H., Hughes, J. P., Kokubun, M., & Porter, F. S. 2006, a poster presentation at Suzaku Conference (2006) held in Kyoto
- Wang, L., Howell, D. A., Höflich, P., & Wheeler, J. C. 2001, ApJ, 550, 1030
- Winkler, P. F., & Petre, R. 2006, astroph/0608205